Dendritic signal integration in a *Drosophila* Mushroom Body Output Neuron (MBON) essential for learning and memory

Omar A. Hafez [*†] Benjamin Escribano [*‡] Rouven L. Ziegler[‡] Jan J. Hirtz[§]
Ernst Niebur[†¶] Jan Pielage[‡‖]

December 6, 2020

Abstract

The ability to associate neutral stimuli with either positive or negative valence forms the basis for most forms of decision making. Long-term memory formation then enables manifestation of these associations to guide behavioral responses over prolonged periods of time. Despite recent advances in the understanding of the neuronal circuits and cellular mechanisms controlling memory formation, the computational principles at the level of individual information processing modules remain largely unknown. Here we use the *Drosophila* mushroom body (MB), the learning and memory center of the fly, as a model system to elucidate the cellular basis of memory computation. Recent studies resolved the precise synaptic connectome of the MB and identified the synaptic connections between Kenyon cells (KCs) and mushroom body output neurons (MBONs) as the sites of sensory association. We build a realistic computational model of the MBON-α3 neuron including precise synaptic connectivity to the 948 upstream KCs innervating the $\alpha\beta$ MB lobes. To model membrane properties reflecting *in vivo* parameters we performed patch-clamp recording of MBON-α3. Based on the *in vivo* data we model synaptic input of individual cholinergic KC-MBON synapses by local conductance changes at the dendritic sections defined by the electron microscopic reconstruction. Modelling of activation of all individual synapses confirms prior results demonstrating that MBON-α3 is electrotonically compact. As a likely consequence of this compactness, activation pattern of individual KCs with identical numbers of synaptic connection but innervating different sections of the MBON-α3 dendritic tree result in highly similar depolarization voltages. Furthermore, we show that KC input patterns reflecting physiological activation by individual odors *in vivo* are sufficient to robustly drive MBON spiking. Our data suggest that the sparse innervation by KCs can control or modulate MBON activity in an efficient manner, with minimal requirements on the specificity of synaptic localization. This KC-MBON architecture therefore provides a suitable module to incorporate different olfactory associative memories based on stochastically encoded odor-specificity of KCs.

1 Introduction

Navigating within a complex environment requires organisms to discriminate between a vast amount of potential rewarding and stressful interactions. Learning to avoid potentially harmful interactions will promote survival of individual animals and is manifested by long term memory (LTM) mechanisms. In recent years, significant progress has been made towards our understanding of the cellular and circuit mechanisms contributing to the formation of learning, short term and long term memory. However, at the computational level it remains unknown how cellular and circuit architecture is setup to efficiently allow the formation and storage of multiple memories in parallel.

Here, we use the *Drosophila melanogaster* mushroom body (MB) as a simplified model system to investigate the computational principles underlying learning and memory. A key advantage of the MB, the learning and memory center of the fly, is the relative simplicity in terms of number and types of neurons compared to the mammalian brain. Numerous studies demonstrated that the MB is required

[*] Equal contribution
[†] Zanvyl Krieger Mind/Brain Institute, Johns Hopkins University, Baltimore, MD 21218, USA
[‡] Division of Neurobiology and Zoology, Department of Biology, University of Kaiserslautern, D-67663 Kaiserslautern, Germany
[§] Physiology of Neuronal Networks Group, Department of Biology, University of Kaiserslautern, D-67663 Kaiserslautern, Germany
[¶] Solomon Snyder Department of Neuroscience, Johns Hopkins University, Baltimore, MD 21218, USA
[‖] To whom correspondence should be addressed: pielage@bio.uni-kl.de

for the acquisition and recall of associative olfactory memories[14, 29, 34, 36, 61] and a wide-variety of genetic tools are available to access and manipulate key cell types within the memory circuitry [16, 17, 28, 30, 31, 33, 40, 45, 53, 58].

The formation of associative olfactory memory within the MB depends on the coincident detection of odors and positive (reward) or negative (punishment) valences. Odor information is transmitted from the antennal lobe via projection neurons (PNs) to the MB. PNs are connected in a stochastic manner to the approximately 2000 KCs per hemisphere resulting in a unique odor representation in all individual flies within the MB [32, 57]. In response to any given odor approximately 5% of KCs are activated [10, 26, 50, 60] and transmit this information to a small number of mushroom body output neurons (MBONs) that are organized within distinct structural and functional modules along the different MB lobes [12, 21, 22, 39, 41, 42, 59]. Interestingly, activity of individual MBONs controls approach or avoidance behavior that is balanced across the MB circuitry to presumably result in zero behavioral output for neutral odors [4, 12, 22]. Valence information regarding concomitant reward or punishment stimuli is transmitted via dopaminergic neurons (DANs) that selectively innervate one of the distinct MBON compartments within the MB lobes [2]. Pairing oder-evoked activity of KCs with valence dependent dopamine release within specific DAN-KC-MBON modules results in synaptic depression or enhancement of KC>Mbon activity. Manifestation of e.g. KC depression in short term or mid term memory (3-6 h after learning) results in a modulation of net MBON output activity and will lead to altered animal behavior in response to the conditioned odor [3, 9, 13, 21, 27, 39]. Recently, genetic tools have been generated that enable genetic tagging of long-term memory engram cells [51] that indicate that modulation of a relatively small number of KCs is sufficient to significantly alter memory recall. Anatomical studies showed that $\alpha\beta$KCs that are essential for memory formation innervate MBON-α3 [2, 55] at the tip of the α lobe that is itself relevant for LTM [4, 44]. Here, we combine anatomical and physiological approaches with computational modelling to create an *in silico* model of MBON-α3 and its KC inputs. Prior electrophysiological [11] and computational [20] studies showed that Drosophila MBONs are electrotonically compact. This indicates that MBONs are capable to compute KC input independently of the locations of individual synaptic contacts within the dendritic tree. To provide insight into the computational mechanisms mediating behaviorally relevant alterations of the KC-MBON synapse it is necessary to determine the physiological parameters underlying this interaction. Here, we combine anatomical and physiological approaches with computational modelling to create an *in silico* model of MBON-α3 and its KC inputs. Our study is based on the published synaptic connectome of the adult Drosophila MB [54, 62] and electrophysiological patch clamp recordings of MBON-α3. We combined these data to generate a realistic fit of the membrane parameters of MBON-α3 and to provide a precise innervation pattern of the 12,770 synaptic contacts of the 948 $\alpha\beta$ KCs that innervate this MBON. Our computational model allows us to provide key insights into the computational principles of sensory information association at this central module for learning and memory.

2 Results

2.1 Electrophysiological characterisation of MBON-α3

MBON-α3 is particularly suitable for computational modeling due to the availability of the complete dendritic reconstruction of MBON-α3 through electron microscopy [55]. We took advantage of the UAS-Gal4 system and a large collection of tissue-specific promoters to fluorescently label MBONs in Drosophila. Out of the available promoters we used MB0832C-Gal4 to specifically label MBON-α3 with a membrane-bound 10XUAS-IVS-mCD8::GFP (figure 1 (A)). With this, we were able to visualize the dendritic input sites, axonal projections as well as the cell soma of MBON-α3 (Figure 1 (A), arrow). This in turn, allowed us to perform fluorescence guided electrophysiological patch-clamp whole-cell recordings with MBON-α3 (Figure 1 (C)&(D)). We ran a collection of standard protocols over five cells. A summary of the collected physiological parameters is provided in Table 1. In a first step, we performed a continuous current-clamp protocol over $60s$ at a sampling rate of $50kHz$ which allowed us to determine an average resting membrane potential of $-56.7 \pm 2.0mV$. The resting membrane potential is in line with previous measurements of MBONs and indicates that we are working with healthy cells [22]. In addition, this allowed us to observe the spontaneous activity of MBON-α3, showing an average firing rate of $12.1Hz$.

In a next step, we performed a current-clamp de- and hyper-polarization protocol where we recorded sweeps for $400ms$ at a $50kHz$ sampling rate. Each sweep started with $0pA$ for $10ms$, which was followed by a current injection $-26pA$ to $32pA$, with $2pA$ increments for $400ms$. With this we were able to observe changes in membrane potentials and to evoke firing of action potentials due to current injection. A condensed example is provided in figure 1 (F). We then performed a current-clamp injection protocol

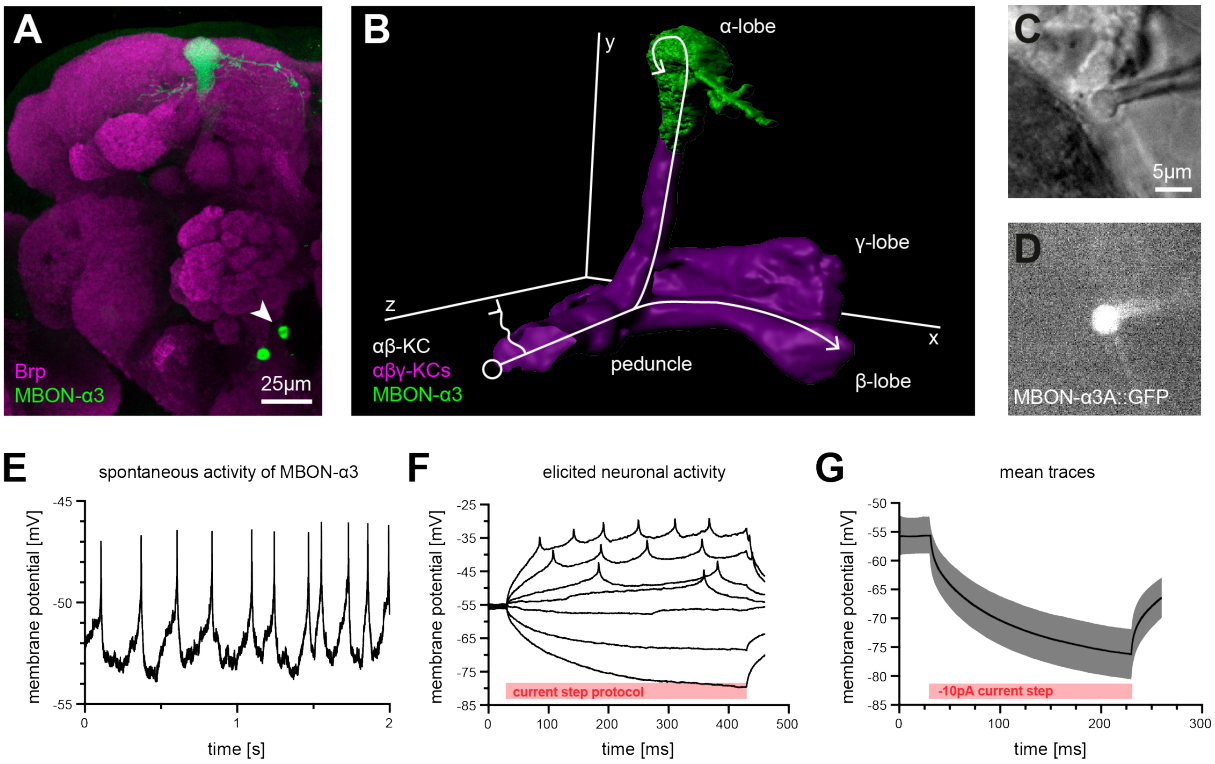

Figure 1: Electrophysiology of MBON-$\alpha 3$. (A) Immunohistological staining of MBON-$\alpha 3$ (green) and bruchpilot (Brp) as a marker for neuronal active zones (magenta). See Section 4.2 for details. (B) Superimposed renderings of MBON-$\alpha 3$ (green) and $\alpha\beta\gamma$-KCs (purple) to illustrate KC-MBON connectivity. An $\alpha\beta$-KC is illustrated in white. (C) Microscopical image of a MBON-$\alpha 3$ soma attached to a patch pipette. The pipette was guided through light microscopy and fluorescence light microscopy (D) Visualisation of GFP expression in MBON-$\alpha 3$ through fluorescense microscopy. Note the pipette to the right of the soma. (E) Spontaneous activity of MBON-$\alpha 3$ measured through patch clamp in the current clamp mode while not injecting any current. (F) Elicited neuronal activity of MBON-$\alpha 3$ through a step wise increasing injection of $400ms$ long current pulses. Current pulses start at $-10pA$ (bottom) continue with $-6, -2, 0, 2, 6pA$ and end at $10pA$ (top). (G) Mean traces of the induced membrane polarization through a $200ms$ long current injection of $-10pA$. We combined 35 trials of 3 different cells for the characterisation of the membrane time constant τ.

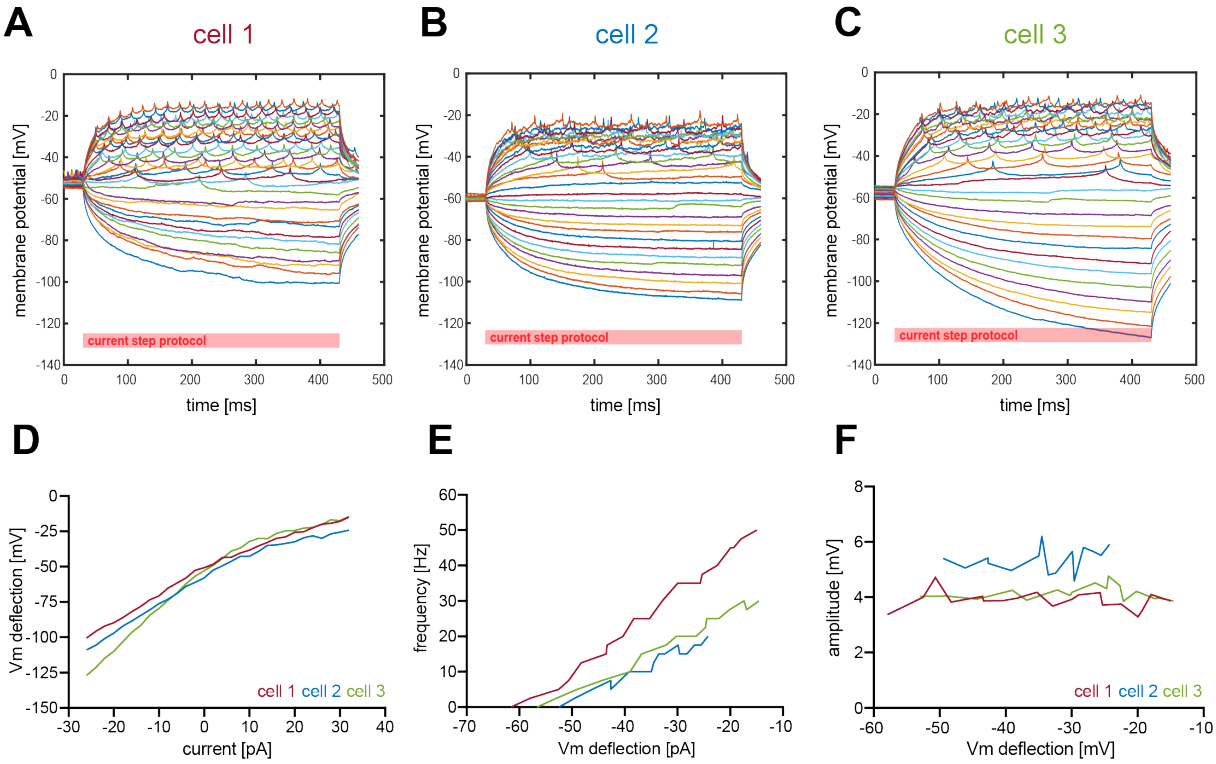

Figure 2: MBON-α3 is a spike frequency adapting neuron. (A) Elicited neuronal activity of MBON-α3 through a step wise increasing injection of $400ms$ long current pulses. Current pulses start at $-26pA$ (bottom) with increasing $2pA$ steps and end at $+32pA$ (top). (B) Second example cell. (C) Third example cell. (D) Relative change of membrane potential through current injection. ΔVm is equal the maximum depolarisation minus resting membrane potential. (E) Correlation between frequency of action potential firing and injected current. The frequency is composed of the action potentials per second. (F) Relative change of spike amplitude through current injections. Spike amplitude equals the peak of the highest action potential minus the baseline.

to determine the membrane time constant as τ_m of $15.6 \pm 2.3ms$. In this protocol we recorded 35 sweeps per cell, where a $10pA$ current pulse was injected for $100ms$ at a sampling rate of $20kHz$. We provide an average of 105 traces from 3 cells in figure 1 (G), with the standard deviation in grey. The raw data from this experiment are provided in the supplement (figure S1). Finally, we performed a voltage-clamp step protocol without compensation of the series resistance. We recorded at $20kHz$ while applying a $5mV$ voltage step for $100ms$, allowing us to calculate the membrane resistance as $R_{membrane} = 926 \pm 55M\Omega$. This is a rather high membrane resistance compared to similar sized neurons which makes the neuron highly excitable since small currents can be sufficient to cause substantial changes in the membrane potential [18] (+Sakmann 2009). However, the observed spontaneous amplitude of action potentials is rather small and similar to previously reported amplitudes [22]. Such small amplitudes may be a result of the unipolar morphology of the neuron in which signal propagation may bypass the soma (figure 2 (A) [18]). In addition, we measured the membrane capacitance as $C_{membrane} = 16.76 \pm 1.90pF$, which classifies this cell as a mid-sized neuron [18, 19] (+Grunewald 2003). These values and the tunability of the MBON-α3 are in good agreement with prior recordings of a different class of MBON and of other central neurons in Drosophila that differ significantly from larger vertebrate neurons to their unipolar organization [23].

In order to gain more insight into how MBON-α3 reacts to an increasing input current we performed multiple analyses of three example cells from the current-clamp de- and hyper-polarization protocol (figure 2 (A)-(C)). For this, we measured in each individual stimulation the absolute deflection, the action potential firing frequency and the amplitude of action potentials. Thereby, we found that in all three cells the absolute deflection of the membrane potential is similarly and consistently rising with increasing current injection (figure 2 (D)). Next, we found that the action potential firing frequency is gradually elevated with an increasing membrane potential deflection (figure 2 (E)). However, with an increase in membrane potential deflection we did not observe any significant alternation in action potential

amplitudes (figure 2 (F)). Considering the current understanding of signal transduction in neurons and the "all or nothing" nature of action potential triggering, this finding fits the concept. Through the in depth analysis electrophysiological recordings we identified MBON-α3 as a spike frequency adapting neuron. Taken together, this data characterizes the physiology of MBON-α3 and builds a solid foundation to equip a structural *in silico* model with realistic passive membrane properties.

2.2 Constructing an *in silico* model of MBON-α3

To construct an *in silico* model of MBON-α3 (figure 3 (B) & (C)) using linear cable theory [37, 38] and an electron microscopy-based reconstruction of MBON-α3 from *Drosophila* (Fig. 4 (A)&(A')) [55, 62] we used the NEURON simulation environment [25]. We subdivided the dendritic input tree into 4,336 different linear sections, 3,121 of which are postsynaptic to one or more of the 12,770 synaptic contacts from KCs (figure 3 (B)) as determined from the published vector data [54, 62] (figure 3 (B)). However, this reconstruction did not determine the morphology of the MBON soma or axonal projections. The dimensions of the former were determined by light microscopy (Fig. 1A), and the geometry of the MBON-α3 axon and synaptic terminals were estimated based on the electronic microscopic reconstruction of a second MBON-α3, see Section 4.4. With this, we constructed a combination of the dendritic input tree with several attached sections that mimic all the neuronal processes. For the details about morphology and section length see table S2 and figure S2.

In previous simulations of *Drosophila* neurons, the kinetics of membrane polarisation due to current injections were adjusted to *in vivo* measurements through a fitting procedure [18]. We performed the analogous current-clamp injection protocol *in silico* by injecting a $-10pA$ current for $200ms$ at the soma, while recording the membrane potential (figure 3 (D)). At the same time we defined the boundaries of the passive membrane parameters within NEURON's PRAXIS (principle axis) optimization algorithm. From this, we were able to use the neuron's experimentally defined passive membrane properties (table 1). We determined the biophysical parameters of the neuron by step-wise increasing current injections and, by recording the neuronal voltage traces, Fig. 4D, we were able to fit the membrane parameters of our model neuron, Fig. 3D,G. The biophysical parameters that resulted from the fitting procedure are provided in the supplement (S3). This procedure resulted in a membrane kinetics that closely resembles *in vivo* current injection of $-10pA$ with a mean squared error between model and measured data of $0.0480917mV^2$.

The resulting trace of the modelled current injection was then normalised (figure 3 (E)) and the traces from the *in vivo* recordings were normalised and averaged (figure 3 (F)). The two normalised traces are overlayed in Figure 3 (G) and were found to be highly correlated, Spearman's correlation coefficient $r = 0.9976$. This excellent agreement validates the use of linear cable theory as a model for this neuron. Taken together, our results demonstrate that the *in silico* MBON-α3 is a highly realistic model of the changes in membrane potential due to current injections into its biological counterpart.

2.3 Computational analysis of KC-MBON interactions

We first simulated input from individual KC-MBON synapses as current injections into precisely (μm scale) identified local dendritic sections. Figure 3A illustrates our simulation paradigm. KC to MBON synapses are believed to be cholinergic, their reversal potential was measured [52] as 8.9mV and synaptic time constant $\tau_s = 0.44ms$. Individual synaptic contacts are simulated as alpha functions ($g_{max}(t-t_i)\times\exp(-(t-t_i-\tau_s)/\tau_s)$) where t_i is the time of the incoming spike and $g_{max} = 1.56 \times 10^{-11}S$, chosen to obtain response levels in agreement with observations, below. The average number of synaptic contacts from a KC to this MBON is 13.47 [54], see Fig. 4C for the distribution of this number for all 948 KCs. For various input patterns to the dendrite, described below, we "record" the cell response in three locations shown in Fig 4A: in the dendrite next to the synapse (red), in the soma (blue) and at the proximal neurite (green) at the base of the dendritic tree, possibly the location where the action potential is initiated.

In the first simulated experiment, each of the 3,121 dendritic sections which receive KC synaptic innervation individually receives an alpha-function conductance change as described, resulting in the voltage excursions shown in Fig 4C. We then analysed the distribution of amplitude per stimulated synapse in the three different sampling sites.

Two features are notable: (1) voltage excursions in the dendrite are faster and substantially larger than in the proximal neurite and soma, and (2), voltages in the latter are much less variable than in the dendrite (figure 4 (D)). This "compactification" or "democratization" of synaptic inputs can be understood from the dendritic geometry. In addition, we observed a voltage attenuation of 75.99% at the soma (figure 4 (FE)). Strikingly, the attenuation does not correlate with the distance between the dendritic input site and the soma (figure 4 (E)).

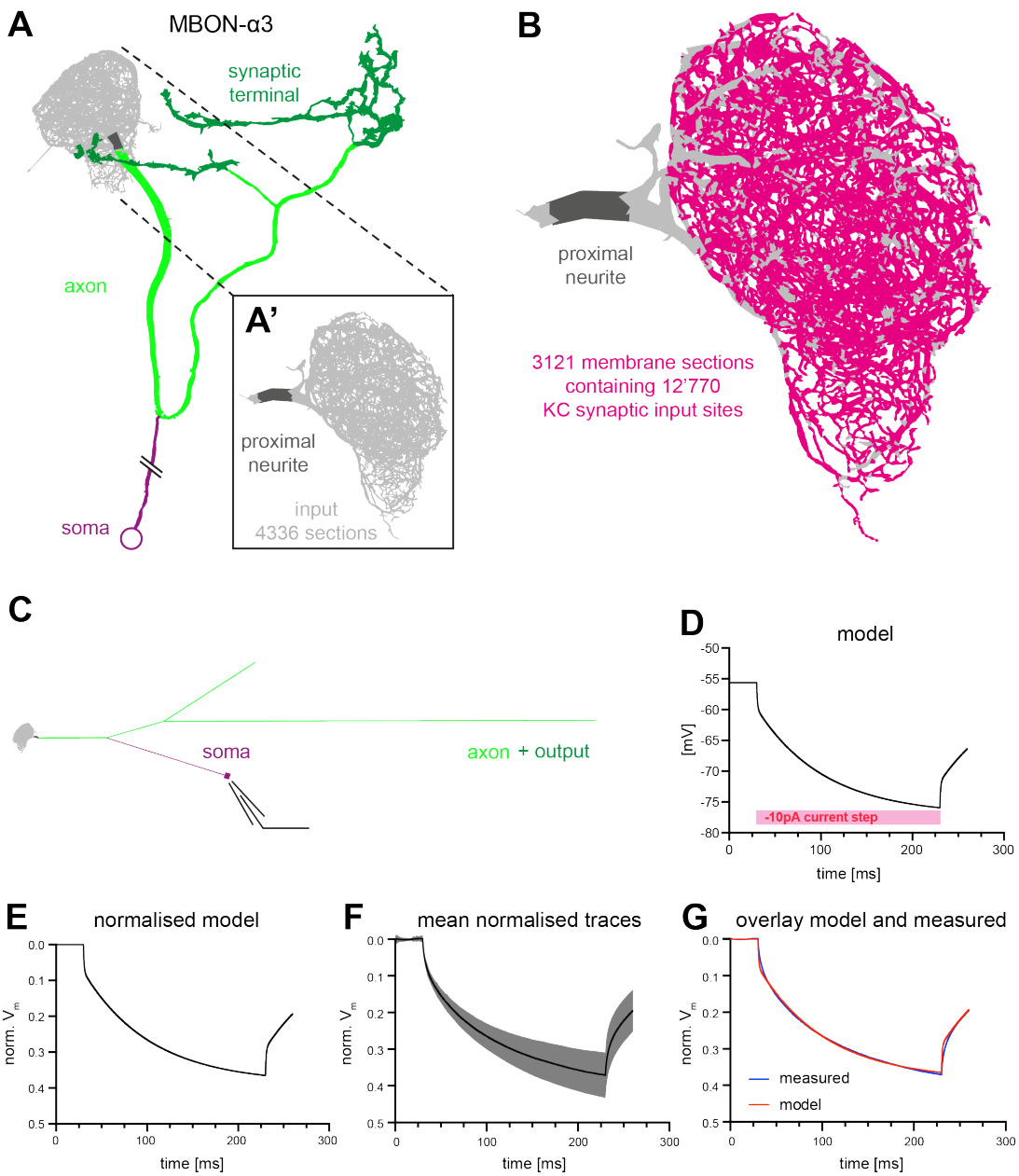

Figure 3: Construction of a computational model simulating MBON-α3-A. (A) Electron microscopy based reconstruction of MBON-α3. Data was obtained from NeuPrint [56] and visualised with NEURON (Citation?). MBON14 (ID 54977) was used for the dendritic architecture (A') and MBON14(a3)R (ID 300972942) was used to characterize the axon and synaptic terminal (A). Axonal section (light green) spans from dendritic input sites (grey) to synaptic terminal (dark green). Soma and extended joint section (purple) are connected to the axonal section for illustration. The precise length of this section and location of the soma are not reconstructed. (A') Magnified and rotated section of the dendritic input sites of MBON-α3. The proximal neurite (dark grey) is connecting the axonal section with the dendritic input sites. In total 4336 membrane sections are defined (light grey) (B) Magnified section of the dendritic input sites. All 3121 membrane sections that are containing 12,770 synaptic input sites are colorized (magenta). (C) *In silico* model of MBON-α3. We appended 5 segments to the proximal neurite of the dendritic section. They account for the total length of the axon and synaptic terminal (light green) as well as soma and extended joint section (purple). (D) Modelled elicited membrane polarization through injection of a $200ms$ long square-pulse current of $-10pA$ at the soma, resulting in a depolarization of the membrane potential. (E) Normalised trace of the model. (F) Normalised and averaged traces (black) with (grey) standard deviation of the measured depolarisation from figure 1 (G). (G) Overlay of normalised induced depolarisation from model (red) and measurement (blue). The model was fitted to the measured normalised mean traces with a mean squared error between model and measured data of $0.0480917mV^2$. We performed a two tailed nonparametric Spearman correlation with a confidence interval of 95% between the two data sets. r=0.9976 and a p=<0.0001

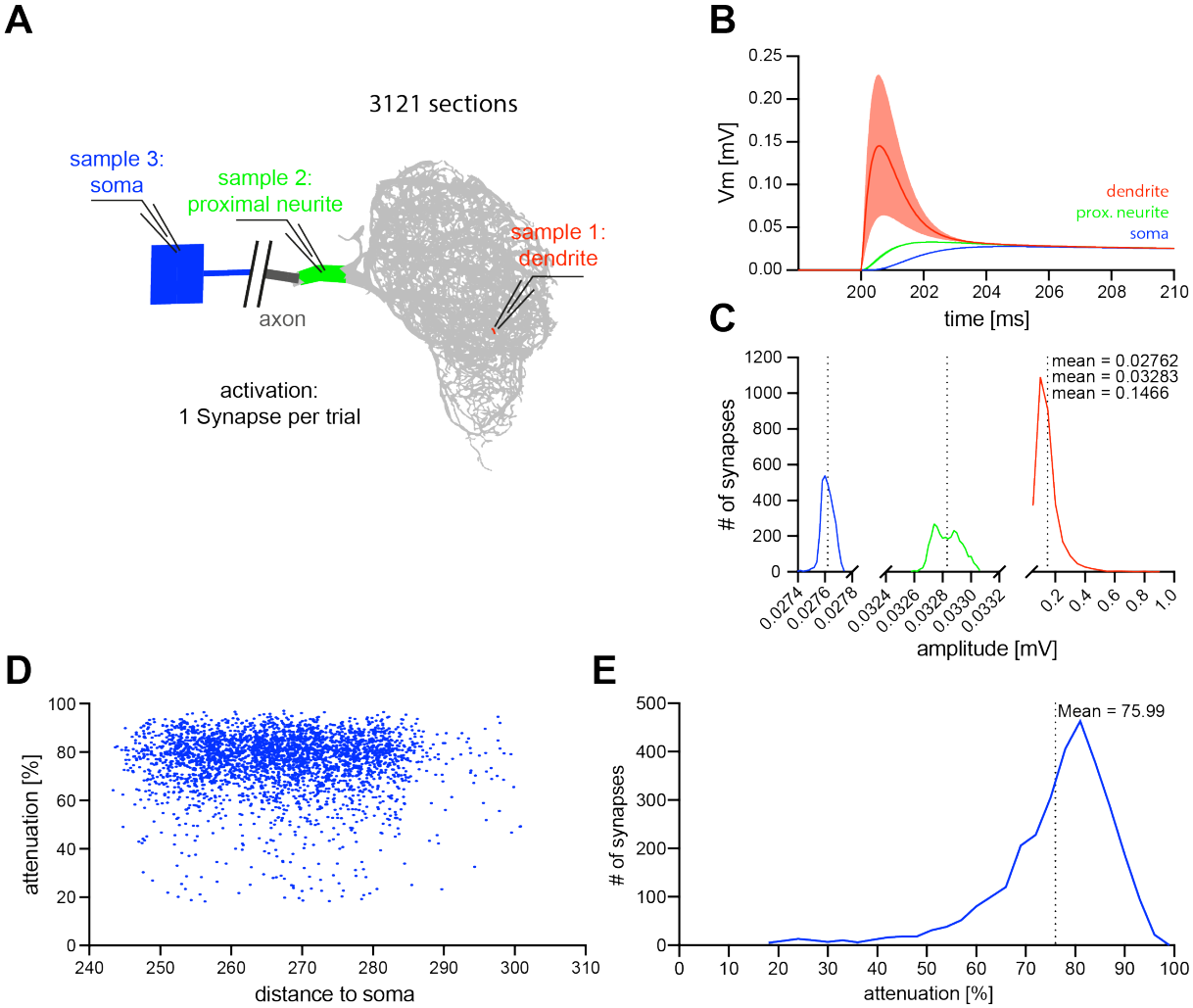

Figure 4: Voltage attenuation in MBON-α3. (A) Scheme of simulated recordings in the dendritic segment (red), proximal neurite (green) and soma (blue). Colors also apply to B,C. (B) Mean voltages with standard deviation from 3121 synaptic activations. (C) Distribution of the measured amplitude per synapse. (D) Correlation of the measured distance to the soma with the percent of voltage attenuation in the soma for each synaptic section. (E) Distribution of the percentage of voltage attenuation in the soma per synapse.

Parameter	Mean ±SEM
$V_m[mV]$	-56.7 ±2.0
$R_s[M\Omega]$	63.7 ±9.7
$R_{in}[M\Omega]$	990 ±58
$R_m[M\Omega]$	926 ±55
$R_{seal}[M\Omega]$	1100 ±45
$\tau[ms]$	15.6 ±2.3
$C_m[pF]$	16.76 ±1.90
$C_{specific}[\mu F/cm^2]$	0.272 ±0.031
$C_{passive}[S/cm^2]$	0.0000178 ±0.0000011

Table 1: Summary of passive membrane properties of MBON-α3, calculated from electrophysiological measurements.

We then repeated the same simulation but, instead of activating one segment at a time, we activate all synapses of each of the KCs, one at a time (figure 5 (A)). In Fig 5B and B' we show the resulting traces of the simulations. Since the number of synaptic contacts per KC varies widely, from 1 to 27 (plus one outlier with 38 contacts), Fig 5G, we observe a wide range of voltage excursions (note the outlier in B,B',C,E,G). However, the neuron is firmly in the small-signal operation mode, as can be seen by the highly linear relation between the voltage excursion and the number of synapses per KC, Fig 5E. Activating a single KC leads to a voltage excursion at the soma with a mean of 0.37mV, Fig 5G, in agreement with the mean of the observed somatic voltage excursion in a population of MBONs [24].

Given that $\approx$ 5% of all 984 KCs are typically activated by an odor, we next simulated voltage excursions in the soma resulting from the simultaneous activation of sets of 50 randomly selected KCs [10, 26], with all of their synaptic contacts localized at the locations known from EM [54] (figure 6 (A)). In Fig 6B and B' we show the resulting traces of the simulations. Figure 5B' shows the voltage distribution due to the activation of individual odors (each corresponding to 50 randomly selected KCs), with a mean of 15.24mV, Fig 5E. Remarkably, input from all odors leads to similar voltage with little variation and, furthermore, comparison with Fig 2A,D and C shows that this voltage excursion is sufficient to reliably generate action potentials. This suggests that odor-induced MBON activity is likely governed by input strength (number and/or conductances of synaptic contacts) while the positions of KC input synapses are largely irrelevant. This result is consistent with the known sparse, random code by which odors are represented by KCs and it allows the association of arbitrary odors with arbitrary behaviors. We also investigated sensitivity of MBON responses to KC input by repeating the same simulation but now activating only 75% of KC-MBON synapses, randomly selected for each KC. We found that the MBON voltage excursion was significantly reduced (two-tailed t-test, p <0.0001), see Fig 6E. Given the linear relation between MBON voltage and firing rate, Fig 2, this change in its input will be reflected in substantial changes in its output. Relatively small changes in the action potential frequency may be what the animal uses as a read-out and it may be behaviorally relevant.

3 Discussion

Changes at the KC-MBON synapse can lead to altered MBON output and account for adaptive memory in *Drosophila* [41]. Despite the publication of a large number of studies on learning and memory in *Drosophila*, the precise mechanisms of synapse modulation and the impact in MBON output remain unclear. Here, we provide a first computational approach to model anatomically correct KC and MBON interactions at single synapse resolution.

Calcium imaging of MBONs after conditioning has revealed that odor induced MBON output can be tuned in two directions [8, 22, 39, 44, 48]. However calcium sensitive dyes are known to have low temporal resolution, thus they are not suitable to draw conclusions about action potential firing. Electrophysiological recordings of MBON-γ1pedc have shown that presentation of an aversively conditioned odor elicits activity with a reduced firing frequency [22]. Here, through electrophysiological recordings, we found that MBON-α3 is a spike frequency adapting neuron as well. Calcium imaging has revealed that this neuron increases its output upon presentation of an appetitively trained odor [44]. Thus, we hypothesise that appetitive training increases, and aversive training decreases the firing frequency of MBON-α3 upon presentation of the conditioned odor. Interestingly, this tuning directions is the opposite of what was reported for MBON-β'2mp and MBON-$\gamma5\beta$'2a [39]. Hence, it is still unclear how dopamine signaling can result in two different modes of synaptic tuning. Recent studies have observed an increased representa-

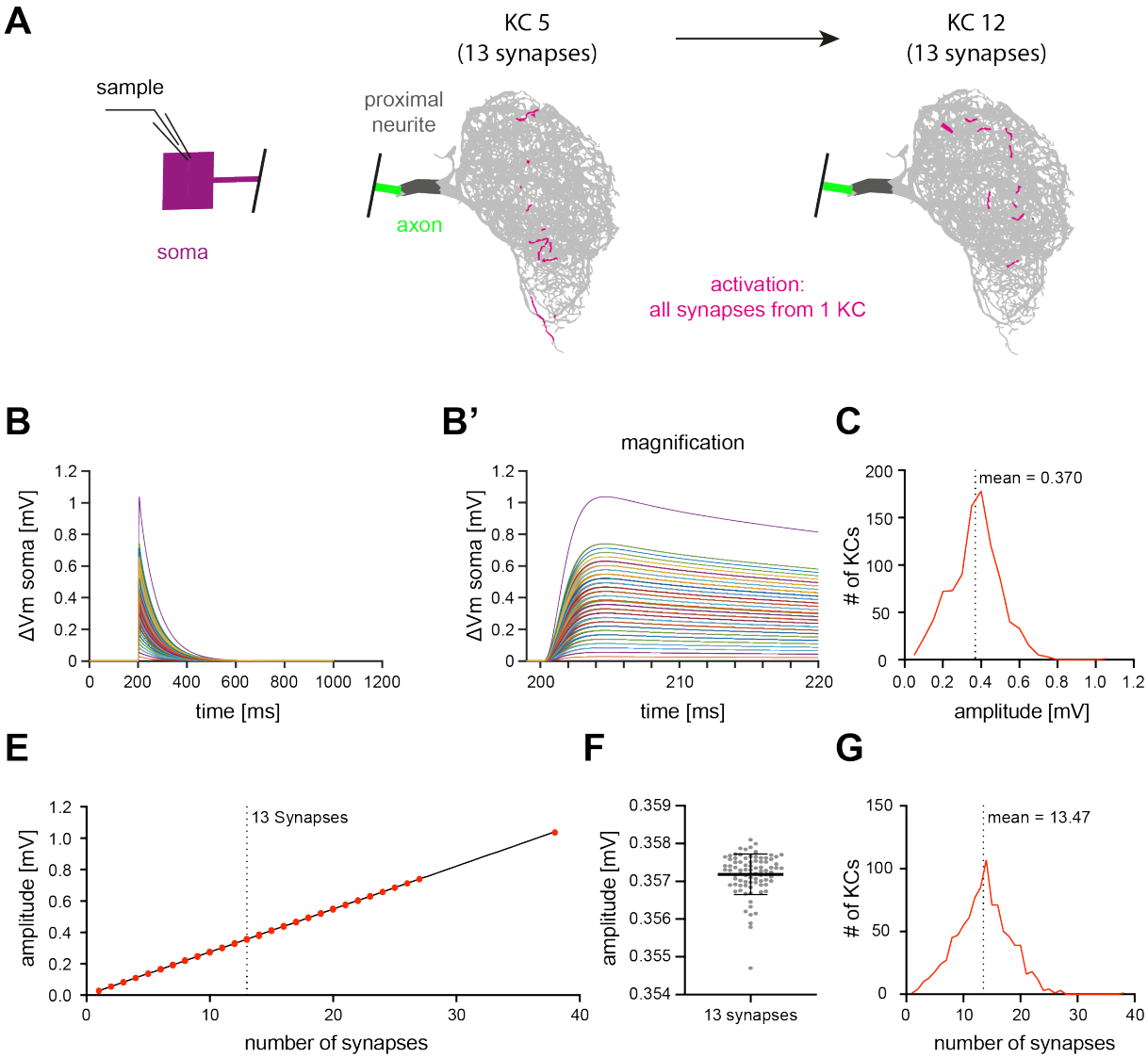

Figure 5: MBON-α3 is electrotonically compact. (A) Scheme of the simulatd recordings in the soma (purple) and simulated activations of single KCs (magenta). (B) Membrane potential traces from simulated activation of all 948 KCs. (B) Same, but magnified section. (C) Correlation between the amplitude and activated KC. (E) Distribution of the amplitude per number of activated synapses. (F) Distribution of amplitude from the activation of KCs with 13 synapses. (G) Distribution of the number of synapses per KC.

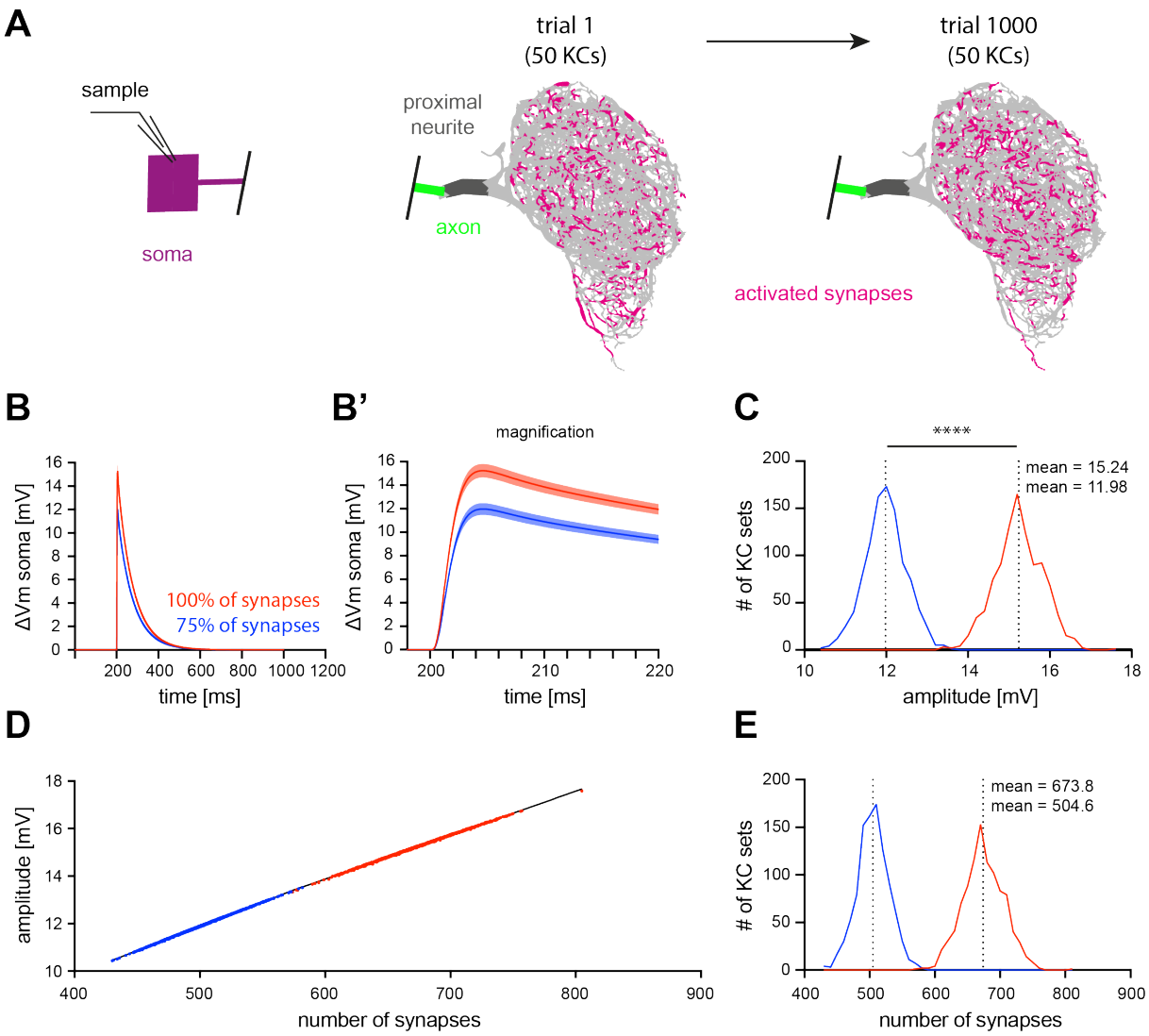

Figure 6: Simulated activations of MBON-α3 through random combination of 50 KCs. (A) Scheme of the simulated recordings in the soma (purple) and simulated activations of 50 KCs (magenta). Each trial is a combination of different KCs, imitating the strenght of an odor input. The strenght of actiovation was altered through activation of 100% versus 75% of synapses. (B) Overlay of mean voltages with standard deviation from activation of 1000 different sets of 50 KCs with 100% (red) or 75% (blue) of synapses. (B') Same but magnified section. (C) Distribution of amplitude per KC set for the activation of 100% (red) and 75% (blue) of synapses. (D) Correlation between number of activated synapses in each set and the elicited amplitude. With 100% (red) and 75% (blue) of activated synapses. (E) Distribution of the number of activated synapses per KC set. Again 100% (red) and 75% (blue).

tion of stimuli in KCs which was mediated through electrical synapses [49]. Furthermore, conditioning induced a functional decorrelation of calcium traces in KC lobes [6, 15]. In short, KCs could be recruited to participate in the representation of a stimulus and increase their synaptic input while on the other hand synaptic modulations can decrease synaptic input at the KC-MBON synapse. Therefore, it is quite possible that two distinct cellular mechanisms are involved in compartmentalized tuning of stimulus specific KC-MBON interactions. Fortunately, with the *in silico* model that was established in this study, we have the opportunity to test both mechanism individually and in combination.

Here, we have used vector data of synapses and dendritic arborizations from the EM based connectome to generate a structural model of MBON-α3 [55]. In addition we have calibrated the model with *in vivo* recordings from MBON-α3. Fitting the model with real data allowed us to obtain nearly identical membrane deflections through a current injection of $-10pA$ at the soma. Those results support our assumption that the model is capable of simulating realistic synaptic inputs and their effect on the MBON membrane potential. In addition, the precise reconstruction of the synaptic locations enables simulations with single synapse resolution. However, the model is restricted to passive biophysical parameters including membrane conductance, cytoplasmic resistivity, and capacitance. Active (nonlinear) voltage gated ion channels are not included. As a consequence only effects on the membrane potential and de- or hyper-polarisation could be observed. This linear model seems to be an excellent approximation for the dendritic tree, as shown by the close agreement between experimentally observed voltage excursions resulting from controlled current injections and their simulated equivalents, see figure 3 G. However, the equations are clearly nonlinear in the description of the axonal parts of the neuron. Thus, excluding active parameters from the model may lead to the observation of artefacts due to nonlinearities in the dendrites or interactions between dendrites and axon. While the potential contributions of nonlinear currents are currently unclear, it is known that voltage-gated Na^+ channels in active *Drosophila* neurons are localized to axonal initial segment-like regions [46] and would therefore not play a role in dendritic processing of olfactory and valence cues.

Our model allows new insights into dendritic signal integration and its transformation into membrane potential deflection. It is a powerful tool that allows for a quantitative explanation of synapse-specific manipulations and recordings of the KC-MBON synapses. In addition, compared to conventional neuroscientific approaches, the spatial and temporal resolution of this model remains unmatched.

4 Materials and methods

4.1 Fly Stocks

Flies were reared on standard fly food at 25°C and 65% humidity. Following stocks were used in this study: 10XUAS-IVS-mCD8::GFP [43] (BDSC 32186), MB082C-Gal4 [1] (BDSC 68286).

4.2 Immunohistochemistry

Male flies expressing GFP in MBON-α3 were fixed for 3.5h at 4°C in 4% PFA containing PBST (0.2% Triton-X100). Flies were then washed for at least 3 x 30 min at RT in PBST before dissection. Dissected brains were then labelled with primary antibodies (rabbit anti-GFP (A6455, Life technologies, 1:2000) and mouse anti-Brp nc82, Developmental Studies Hybridoma Bank, Iowa, 1:200) for two nights at 4°C. After incubation, brains were washed at least 6 x 30 min in PBST. Secondary antibodies (Alexa488 (goatαrabbit) and Alexa568 (goatαmouse) coupled antibodies, Life technologies, 1:1000) were applied for two nights at 4°C. After a repeated washing period, brains were submerged in Vectashield (Vector Laboratories), mounted onto microscope slides and stored at 4°C.

Images were acquired using a confocal scanning microscope (Zeiss LSM 710) and a 25x (Zeiss Plan-NEOFLUAR, NA 0.8 Korr DIC) oil objective. Raw images were projected with Fiji [47] and cropped in Photoshop (Adobe). Uniform adjustments of brightness and contrast were performed.

4.3 Electrophysiology

Flies were flipped 1d after hatching to obtain 3-5d old flies. Due to the inconvenient location of the soma we performed *ex vivo* recordings of the brain. For preparation, flies expressing GFP in MBON-α3 were briefly anesthetized on ice before removing the entire brain from the head. The preparation was performed in oxygenated (95% O_2 and 5% CO_2) high glucose ($260mM$) extracellular saline. As described previously, the brain was incubated for $30s$ in $0.5mg/ml$ protease (from Streptomyces griseus, CAS# 90036-06-0, Sigma) containing extracellular saline [**?**]. The brain was then transferred to standard

extracellular saline [?] (in mM: 103 $NaCl$, 3 KCl, 5 TES, 10 trehalose, 260 glucose, 7 sucrose, 26 $NaHCO_3$, 1 NaH_2PO_4, 1.5 $CaCl_2$, 4 $MgCl_2$, pH 7.3, $280-290mOsmol/kg$ adjusted with sucrose). For physiological recordings, the brain was transferred to a glass bottom chamber with continuously perfused ($2ml/min$) oxygenated standard extracellular saline and held in place by a custom made platinum frame. All recordings were performed at room temperature.

We used glass capillaries (GB150 (F-)-10P, Science Products, Hofheim, Germany) and a horizontal puller (Flaming Brown Micropipette Puller P-1000, Sutter instruments, Novato, USA) to obtain pipettes with a resistance of $7-10M\Omega$. For recordings, patch pipettes were filled with internal solution [35] (in mM: 140 K-aspartate, 10 HEPES, 4 Mg-ATP, 0.5 Na-GTP, 1 EGTA, 1 KCl, pH 7.29 adjusted with KOH, $265mOsmol/kg$). Whole-cell recordings were made using the EPC10 amplifier (HEKA, Germany) and the PatchMaster software (HEKA, Germany). Signals were low-pass filtered at $3kHz$, and digitized at $10kHz$ via a digital-to-analog converter. The liquid junction potential of $13mV$ was corrected online. Patch pipettes were guided under visual control with an upright microscope (BX51WI; Olympus) equipped with a 60x water immersion objective (LUMPlanFl/IR; Olympus) and a CCD camera (Orca 05G, Hamamatsu). GFP signal of target cells was visualized through fluorescence excitation (100W fluorescence lamp, Zeiss, Germany), and a dual-band emission filter set (512/630 HC Dualband Filter GFP/DsRed, AHF Analysentechnik, Germany). We used GFP expression in soma and neurite to identify MBON-α3 neurons. During recordings, the fluorescence excitation was shut off to minimize phototoxic effects. The complete setup was mounted on an air damped table while being shielded by a faraday cage. Series resistance was maintained below $90M\Omega$ and compensated for up to 35% through the amplifier's compensation circuitry. In current-clamp mode, cells were held at a baseline of $-60mV$ to measure the relevant parameters for the model. Signals were recorded with a sample rate of $20kHz$ or $50kHz$ and low-pass filtered at $5kHz$.

To determine passive electrical membrane properties and qualitative patch characteristics a series of standard protocols were performed:

VCstep without compensation. In voltage-clamp mode, a voltage-step ($100ms$, $5mV$) is applied without compensating the series resistance. The corresponding current trace was then used to determine R_{series}, R_{input} and $R_{membrane}$ with Igor Pro (WaveMetrics).

CCdehyper. In current-clamp mode, a step-protocol was performed and recorded at $50kHz$. Each sweep starts with $0pA$ for $10ms$, which is followed by a current injection ($-26pA$ to $32pA$, with $2pA$ increments) and a step duration of $400ms$. The resulting changes in membrane potential and induced action potentials were then analyzed and plotted with Matlab (MathWorks). The maximum depolarisation was calculated as a mean of the last 70 sample points of the stimulation in each trace. The resting membrane potential was calculated as the mean of the first 500 sample points before the stimulation in each trace. The absolute action potential was measured as maximum of each trace. The relative action potential amplitude resulted from subtracting the baseline from the absolute value. The baseline resulted from the mean of a 400 sample points window, starting 700 sample points upstream of the maxima in each trace.

CCcontinuous. In current-clamp mode, no current was injected through out a $60s$ recording at $50kHz$. The resting membrane potential was determined as the mean of the baseline in the recording with Igor Pro and spontaneous activity was plotted with Matlab.

CCinject. In current-clamp mode, a short current pulse ($-50pA$, $100ms$) was injected and recorded at $20kHz$. We performed 35 iterations per cell. The resulting change in membrane potential was used to determine $\tau_{membrane}$ with a single exponential fit in Igor Pro. Averaging, normalisation (V_m-V_{m0}/V_{m0}) and plotting was performed with Matlab. This data was used to perform the model fitting. The baseline (V_{m0}) resulted from the average of the sample points before stimulation.

Cells displaying a resting membrane potential higher than $-45mV$ and/or a $R_{membrane}$ smaller than $600M\Omega$ were excluded from the analysis.

4.4 Computational Model

Morphology data for the Drosophila MBON-α3-A was originally characterized using scanning electron microscopy [56] and for the present study obtained from the "mushroombody" dataset hosted on the database neuPrint (https://neuprint-examples.janelia.org/; cell ID 54977). These data describe the structure of its dendritic arborization throughout the MBON α3 compartment (Fig. 3A'), with coordinates specified at 8nm pixel resolution and converted to μm for model implementation. The reconstruction is limited to the portion of the neuron in the mushroom body, not including its soma and axon. The geometry of the axon was determined by investigating a separate MBON, MBON14(a3)R (Fig. 3A), obtained from neuPrint's "hemibrain:v1.1" dataset (https://neuprint.janelia.org/; cell ID 300972942). The axon and synaptic terminal of this neuron were approximated as five separate sections, distinguished by the

major branch points identified in the electron microscopic reconstruction. Each section was characterized by its total length and average diameter and divided into segments to maintain the average section length of that region in the original reconstruction (Fig. S2). They were then appended to the MBON-α3-A proximal neurite as individual linear segments. The dimensions of the soma were characterized by our light microscopic images of MBON-α3-A (Fig. 1A). Synaptic locations of the KC innervation of this MBON-α3-A were also obtained from neuPrint's "mushroombody" dataset. MBON-α3-A is innervated by 948 distinct KCs, forming a total of 12,770 synapses with an average of 13.47 synapses per KC [56].

Electrophysiological properties of the neuron were determined by fitting the model response to recorded data, an approach consistent with prior work modeling *Drosophila* central neurons [18]. Somatic voltage excursions in response to 200ms current injections of -10pA were recorded *in vivo* (Fig. 1G). This current injection was replicated *in silico* and the membrane potential change at the soma was fit to our recorded data by varying the cell's cytoplasm resistivity, specific membrane capacitance, and passive membrane conductance. The fitting was performed using NEURON's principle axis optimization algorithm, where parameters were tuned until the computed voltage excursion at the soma matched our electrophysiological recordings. The model optimization searched parameter space to minimize an error function defined as the square differences between the averaged experimental responses to current pulses (Fig. 1G) and the computed model responses (Fig. 3D). The fitting was then verified by normalizing both the model and experimental voltage excursions and performing two-tailed nonparametric Spearman correlation. The model was first allowed to equilibrate for 30ms, after which the 200 ms current pulse was initiated. The region of data used for the the fitting ranged from 32.025ms to 228.03ms, excluding approximately the first and last 2ms of current injection. The domain of the parameter space was restricted to physiologically plausible values: 0.5μF/cm^2 to 1.5μF/cm^2 for specific membrane capacitance, 1E-7S/cm^2 to 1E-4S/cm^2 for passive membrane conductance, and 30Ωcm to 400Ωcm for cytoplasm resistivity. The final values for each parameter (Table S3) are well within these margins. Resting membrane potential and the leak current reversal potential were set at -55.64mV based on the initial conditions of the recorded data to which the model was fit.

Synapses were modeled as localized conductance changes described by alpha functions. KC innervation of MBON-α3-A was determined to be cholinergic [56]. Currents recorded in *Drosophila* KCs were demonstrated to have a reversal potential of 8.9mV and a rise time to maximal conductance of 0.44ms [52]. The maximal conductance for the synapses was set at $1.5627 * 10^{-5} \mu S$, the value determined to achieve the target MBON depolarization from monosynaptic KC innervation [24].

All simulations were performed using the NEURON 7.7.2 simulation environment [25] running through a Python 3.8.5 interface in Ubuntu 20.04.1. The morphology data divided the MBON-α3-A dendritic tree into 4336 small sections averaging 1.03μm in length and 0.29μm in diameter. With the added sections describing the axon, synaptic terminals, and soma, the model contained 4342 sections averaging 1.24μm in length and 0.29μm in diameter. Each dendritic section was automatically assigned an index number by NEURON. Each of these sections was modeled as a piece of cylindrical cable, with connectivity specified by the neuron's morphology. Passive leak channels were inserted along the membrane of the dendrite sections as well as throughout the axon and soma. The coordinate location of each KC synapse was mapped to the nearest section of the MBON dendrite, and the conductance-based synapse model was implemented in the center of that section. Simulations were performed in which each synapse-containing section was individually activated, followed by additional simulations activating groups of synapses corresponding to single or multiple active KCs. Membrane potential data was analyzed and plotted with MATLAB R2020b (MathWorks) and Prism (GraphPad).

Acknowledgments

Work supported by NSF 1835202, NIH R01DA040990 and NIH R01EY027544

References

[1] Yoshinori Aso, Daisuke Hattori, Yang Yu, Rebecca M Johnston, Nirmala A Iyer, Teri-TB Ngo, Heather Dionne, L F Abbott, Richard Axel, Hiromu Tanimoto, and Gerald M Rubin. The neuronal architecture of the mushroom body provides a logic for associative learning. *eLife*, 3:e10806, December 2014.

[2] Yoshinori Aso, Daisuke Hattori, Yang Yu, Rebecca M Johnston, Nirmala A Iyer, Teri-TB Ngo, Heather Dionne, Lf Abbott, Richard Axel, Hiromu Tanimoto, and Gerald M Rubin. The neuronal architecture of the mushroom body provides a logic for associative learning. *eLife*, 3:e04577, December 2014.

[3] Yoshinori Aso and Gerald M Rubin. Dopaminergic neurons write and update memories with cell-type-specific rules. *eLife*, 5:e16135, July 2016.

[4] Yoshinori Aso, Divya Sitaraman, Toshiharu Ichinose, Karla R Kaun, Katrin Vogt, Ghislain Belliart-Guérin, Pierre-Yves Plaçais, Alice A Robie, Nobuhiro Yamagata, Christopher Schnaitmann, William J Rowell, Rebecca M Johnston, Teri-T B Ngo, Nan Chen, Wyatt Korff, Michael N Nitabach, Ulrike Heberlein, Thomas Preat, Kristin M Branson, Hiromu Tanimoto, and Gerald M Rubin. Mushroom body output neurons encode valence and guide memory-based action selection in Drosophila. *eLife*, 3:e04580, December 2014.

[5] Sandra D. Berger and Sharon M. Crook. Modeling the influence of ion channels on neuron dynamics in drosophila. *Frontiers in Computational Neuroscience*, 9:139, 2015.

[6] Florian Bilz, Bart R.H. Geurten, Clare E. Hancock, Annekathrin Widmann, and André Fiala. Visualization of a Distributed Synaptic Memory Code in the Drosophila Brain. *Neuron*, page S0896627320302178, April 2020.

[7] Alexander Borst and Juergen Haag. The intrinsic electrophysiological characteristics of fly lobula plate tangential cells: I. Passive membrane properties. *Journal of Computational Neuroscience*, 3(4):313–336, December 1996.

[8] Emna Bouzaiane, Séverine Trannoy, Lisa Scheunemann, Pierre-Yves Plaçais, and Thomas Preat. Two Independent Mushroom Body Output Circuits Retrieve the Six Discrete Components of Drosophila Aversive Memory. *Cell Reports*, 11(8):1280–1292, May 2015.

[9] Christopher J Burke, Wolf Huetteroth, David Owald, Emmanuel Perisse, Michael J Krashes, Gaurav Das, Daryl Gohl, Marion Silies, Sarah Certel, and Scott Waddell. Layered reward signalling through octopamine and dopamine in Drosophila. *Nature*, 492(7429):433–437, October 2012.

[10] R. A. A. Campbell, K. S. Honegger, H. Qin, W. Li, E. Demir, and G. C. Turner. Imaging a Population Code for Odor Identity in the Drosophila Mushroom Body. *Journal of Neuroscience*, 33(25):10568–10581, June 2013.

[11] Stijn Cassenaer and Gilles Laurent. Hebbian stdp in mushroom bodies facilitates the synchronous flow of olfactory information in locusts. *Nature*, 448(7154):709, 2007.

[12] Paola Cognigni, Johannes Felsenberg, and Scott Waddell. Do the right thing: neural network mechanisms of memory formation, expression and update in Drosophila. *Current opinion in neurobiology*, 49:51–58, April 2018.

[13] Raphael Cohn, Ianessa Morantte, and Vanessa Ruta. Coordinated and Compartmentalized Neuromodulation Shapes Sensory Processing in Drosophila. *Cell*, 163(7):1742–1755, December 2015.

[14] J. S. de Belle and M. Heisenberg. Associative odor learning in Drosophila abolished by chemical ablation of mushroom bodies. *Science (New York, N.Y.)*, 263(5147):692–695, February 1994.

[15] Felipe Delestro, Lisa Scheunemann, Mélanie Pedrazzani, Paul Tchenio, Thomas Preat, and Auguste Genovesio. In vivo large-scale analysis of Drosophila neuronal calcium traces by automated tracking of single somata. *Scientific Reports*, 10(1):7153, December 2020.

[16] Georg Dietzl, Doris Chen, Frank Schnorrer, Kuan-Chung Su, Yulia Barinova, Michaela Fellner, Beate Gasser, Kaolin Kinsey, Silvia Oppel, Susanne Scheiblauer, Africa Couto, Vincent Marra, Krystyna Keleman, and Barry J Dickson. A genome-wide transgenic RNAi library for conditional gene inactivation in Drosophila. *Nature*, 448(7150):151–156, July 2007.

[17] Florence Friggi-Grelin, H l ne Coulom, Margaret Meller, Delphine Gomez, Jay Hirsh, and Serge Birman. Targeted gene expression inDrosophila dopaminergic cells using regulatory sequences from tyrosine hydroxylase. *Journal of Neurobiology*, 54(4):618–627, January 2003.

[18] N. W. Gouwens and R. I. Wilson. Signal Propagation in Drosophila Central Neurons. *Journal of Neuroscience*, 29(19):6239–6249, May 2009.

[19] Cicely X Gu, Peter F Juranka, and Catherine E Morris. Stretch-activation and stretch-inactivation of Shaker-IR, a voltage-gated K+ channel. *Biophysical Journal*, 80(6):2678–2693, 2001.

[20] Omar Hafez, Benjamin Escribano, Jan Pielage, and Ernst Niebur. Integration of odor-induced activity of Kenyon Cells in an electrotonically compact *Drosophila* Mushroom Body Output Neuron (MBON). b*ioR*χ*iv*, 2019. doi: `10.1.1/jpb001`.

[21] Annie Handler, Thomas G.W. Graham, Raphael Cohn, Ianessa Morantte, Andrew F. Siliciano, Jianzhi Zeng, Yulong Li, and Vanessa Ruta. Distinct Dopamine Receptor Pathways Underlie the Temporal Sensitivity of Associative Learning. *Cell*, 178(1):60–75.e19, June 2019.

[22] Toshihide Hige, Yoshinori Aso, Mehrab N. Modi, Gerald M. Rubin, and Glenn C. Turner. Heterosynaptic Plasticity Underlies Aversive Olfactory Learning in Drosophila. *Neuron*, 88(5):985–998, December 2015.

[23] Toshihide Hige, Yoshinori Aso, Mehrab N Modi, Gerald M Rubin, and Glenn C Turner. Heterosynaptic Plasticity Underlies Aversive Olfactory Learning in Drosophila. *Neuron*, 88(5):985–998, December 2015.

[24] Toshihide Hige, Yoshinori Aso, Gerald M Rubin, and Glenn C Turner. Plasticity-driven individualization of olfactory coding in mushroom body output neurons. *Nature*, 526(7572):258–262, September 2015.

[25] M. L. Hines and N. T. Carnevale. The Neuron Simulation Environment. *Neural Computation*, 9(6), Aug. 1997.

[26] K. S. Honegger, R. A. A. Campbell, and G. C. Turner. Cellular-Resolution Population Imaging Reveals Robust Sparse Coding in the Drosophila Mushroom Body. *Journal of Neuroscience*, 31(33):11772–11785, August 2011.

[27] Wolf Huetteroth, Emmanuel Perisse, Suewei Lin, Martín Klappenbach, Christopher Burke, and Scott Waddell. Sweet Taste and Nutrient Value Subdivide Rewarding Dopaminergic Neurons in Drosophila. *Current Biology*, 25(6):751–758, March 2015.

[28] Arnim Jenett, Gerald M Rubin, Teri-T B Ngo, David Shepherd, Christine Murphy, Heather Dionne, Barret D Pfeiffer, Amanda Cavallaro, Donald Hall, Jennifer Jeter, Nirmala Iyer, Dona Fetter, Joanna H Hausenfluck, Hanchuan Peng, Eric T Trautman, Robert R Svirskas, Eugene W Myers, Zbigniew R Iwinski, Yoshinori Aso, Gina M DePasquale, Adrianne Enos, Phuson Hulamm, Shing Chun Benny Lam, Hsing-Hsi Li, Todd R Laverty, Fuhui Long, Lei Qu, Sean D Murphy, Konrad Rokicki, Todd Safford, Kshiti Shaw, Julie H Simpson, Allison Sowell, Susana Tae, Yang Yu, and Christopher T Zugates. A GAL4-Driver Line Resource for Drosophila Neurobiology. *Cell reports*, 2(4):991–1001, October 2012.

[29] Colleen Kirkhart and Kristin Scott. Gustatory Learning and Processing in the *Drosophila* Mushroom Bodies. *The Journal of Neuroscience*, 35(15):5950–5958, April 2015.

[30] Nathan C Klapoetke, Yasunobu Murata, Sung Soo Kim, Stefan R Pulver, Amanda Birdsey-Benson, Yong Ku Cho, Tania K Morimoto, Amy S Chuong, Eric J Carpenter, Zhijian Tian, Jun Wang, Yinlong Xie, Zhixiang Yan, Yong Zhang, Brian Y Chow, Barbara Surek, Michael Melkonian, Vivek Jayaraman, Martha Constantine-Paton, Gane Ka-Shu Wong, and Edward S Boyden. Independent optical excitation of distinct neural populations. *Nature Methods*, 11(3):338–346, February 2014.

[31] Sen-Lin Lai and Tzumin Lee. Genetic mosaic with dual binary transcriptional systems in Drosophila. *Nature Neuroscience*, 9(5):703–709, April 2006.

[32] Hui-Hao Lin, Jason Sih-Yu Lai, An-Lun Chin, Yung-Chang Chen, and Ann-Shyn Chiang. A Map of Olfactory Representation in the Drosophila Mushroom Body. *Cell*, 128(6):1205–1217, March 2007.

[33] Lindsey J Macpherson, Emanuela E Zaharieva, Patrick J Kearney, Michael H Alpert, Tzu-Yang Lin, Zeynep Turan, Chi-Hon Lee, and Marco Gallio. Dynamic labelling of neural connections in multiple colours by trans-synaptic fluorescence complementation. *Nature communications*, 6(1):501, December 2015.

[34] P. Masek and K. Scott. Limited taste discrimination in Drosophila. *Proceedings of the National Academy of Sciences*, 107(33):14833–14838, August 2010.

[35] Alex S. Mauss, Matthias Meier, Etienne Serbe, and Alexander Borst. Optogenetic and pharmacologic dissection of feedforward inhibition in Drosophila motion vision. *The Journal of Neuroscience: The Official Journal of the Society for Neuroscience*, 34(6):2254–2263, February 2014.

[36] Sean M.J McBride, Giovanna Giuliani, Catherine Choi, Paul Krause, Dana Correale, Karli Watson, Glenn Baker, and Kathleen K Siwicki. Mushroom Body Ablation Impairs Short-Term Memory and Long-Term Memory of Courtship Conditioning in Drosophila melanogaster. *Neuron*, 24(4):967–977, December 1999.

[37] E. Niebur. Electrical properties of cell membranes. *Scholarpedia*, 3(6):7166, 2008.

[38] E. Niebur. Neuronal Cable Theory. *Scholarpedia*, 3(5):2674, 2008.

[39] David Owald, Johannes Felsenberg, Clifford B. Talbot, Gaurav Das, Emmanuel Perisse, Wolf Huetteroth, and Scott Waddell. Activity of Defined Mushroom Body Output Neurons Underlies Learned Olfactory Behavior in Drosophila. *Neuron*, 86(2):417–427, April 2015.

[40] David Owald, Suewei Lin, and Scott Waddell. Light, heat, action: neural control of fruit fly behaviour. *Philosophical Transactions of the Royal Society B: Biological Sciences*, 370(1677):20140211, September 2015.

[41] David Owald and Scott Waddell. Olfactory learning skews mushroom body output pathways to steer behavioral choice in Drosophila. *Current Opinion in Neurobiology*, 35:178–184, December 2015.

[42] Emmanuel Perisse, David Owald, Oliver Barnstedt, Clifford B. Talbot, Wolf Huetteroth, and Scott Waddell. Aversive Learning and Appetitive Motivation Toggle Feed-Forward Inhibition in the Drosophila Mushroom Body. *Neuron*, 90(5):1086–1099, June 2016.

[43] Barret D. Pfeiffer, Teri-T B. Ngo, Karen L. Hibbard, Christine Murphy, Arnim Jenett, James W. Truman, and Gerald M. Rubin. Refinement of Tools for Targeted Gene Expression in Drosophila. *Genetics*, 186(2):735–755, October 2010.

[44] Pierre-Yves Plaçais, Séverine Trannoy, Anja B. Friedrich, Hiromu Tanimoto, and Thomas Preat. Two Pairs of Mushroom Body Efferent Neurons Are Required for Appetitive Long-Term Memory Retrieval in Drosophila. *Cell Reports*, 5(3):769–780, November 2013.

[45] Christopher J Potter, Bosiljka Tasic, Emilie V Russler, Liang Liang, and Liqun Luo. The Q System: A Repressible Binary System for Transgene Expression, Lineage Tracing, and Mosaic Analysis. *Cell*, 141(3):536–548, April 2010.

[46] Thomas A Ravenscroft, Jasper Janssens, Pei-Tseng Lee, Burak Tepe, Paul C Marcogliese, Samira Makhzami, Todd C Holmes, Stein Aerts, and Hugo J Bellen. Drosophila voltage-gated sodium channels are only expressed in active neurons and are localized to distal axonal initial segment-like domains. *Journal of Neuroscience*, 40(42):7999–8024, 2020.

[47] Johannes Schindelin, Ignacio Arganda-Carreras, Erwin Frise, Verena Kaynig, Mark Longair, Tobias Pietzsch, Stephan Preibisch, Curtis Rueden, Stephan Saalfeld, Benjamin Schmid, Jean-Yves Tinevez, Daniel James White, Volker Hartenstein, Kevin Eliceiri, Pavel Tomancak, and Albert Cardona. Fiji: An open-source platform for biological-image analysis. *Nature Methods*, 9(7):676–682, July 2012.

[48] Julien Séjourné, Pierre-Yves Plaçais, Yoshinori Aso, Igor Siwanowicz, Séverine Trannoy, Vladimiros Thoma, Stevanus R Tedjakumala, Gerald M Rubin, Paul Tchénio, Kei Ito, Guillaume Isabel, Hiromu Tanimoto, and Thomas Preat. Mushroom body efferent neurons responsible for aversive olfactory memory retrieval in Drosophila. *Nature Neuroscience*, 14(7):903–910, July 2011.

[49] Wei-Huan Shyu, Wang-Pao Lee, Meng-Hsuan Chiang, Ching-Ching Chang, Tsai-Feng Fu, Hsueh-Cheng Chiang, Tony Wu, and Chia-Lin Wu. Electrical synapses between mushroom body neurons are critical for consolidated memory retrieval in Drosophila. *PLOS Genetics*, 15(5):e1008153, May 2019.

[50] Dominique Siegenthaler, Benjamin Escribano, Vanessa Bräuler, and Jan Pielage. Selective suppression and recall of long-term memories in Drosophila. *PLOS Biology*, 17(8):e3000400, August 2019.

[51] Dominique Siegenthaler, Benjamin Escribano, Vanessa Bräuler, and Jan Pielage. Selective suppression and recall of long-term memories in Drosophila. *PLoS Biology*, 17(8):e3000400, August 2019.

[52] Hailing Su and Diane K O'Dowd. Fast synaptic currents in drosophila mushroom body kenyon cells are mediated by α-bungarotoxin-sensitive nicotinic acetylcholine receptors and picrotoxin-sensitive gaba receptors. *Journal of Neuroscience*, 23(27):9246–9253, 2003.

[53] Sean T Sweeney, Kendal Broadie, John Keane, Heiner Niemann, and Cahir J O'Kane. Targeted expression of tetanus toxin light chain in Drosophila specifically eliminates synaptic transmission and causes behavioral defects. *Neuron*, 14(2):341–351, February 1995.

[54] Shin-Ya Takemura, Yoshinori Aso, Toshihide Hige, Allan Wong, Zhiyuan Lu, C Shan Xu, Patricia K Rivlin, Harald Hess, Ting Zhao, Toufiq Parag, Stuart Berg, Gary Huang, William Katz, Donald J Olbris, Stephen Plaza, Lowell Umayam, Roxanne Aniceto, Lei-Ann Chang, Shirley Lauchie, Omotara Ogundeyi, Christopher Ordish, Aya Shinomiya, Christopher Sigmund, Satoko Takemura, Julie Tran, Glenn C Turner, Gerald M Rubin, and Louis K Scheffer. A connectome of a learning and memory center in the adult Drosophila brain. *eLife*, 6:5643, July 2017.

[55] Shin-ya Takemura, Yoshinori Aso, Toshihide Hige, Allan Wong, Zhiyuan Lu, C Shan Xu, Patricia K Rivlin, Harald Hess, Ting Zhao, Toufiq Parag, Stuart Berg, Gary Huang, William Katz, Donald J Olbris, Stephen Plaza, Lowell Umayam, Roxanne Aniceto, Lei-Ann Chang, Shirley Lauchie, Omotara Ogundeyi, Christopher Ordish, Aya Shinomiya, Christopher Sigmund, Satoko Takemura, Julie Tran, Glenn C Turner, Gerald M Rubin, and Louis K Scheffer. A connectome of a learning and memory center in the adult Drosophila brain. *eLife*, 6:e26975, July 2017.

[56] Shin-ya Takemura, Yoshinori Aso, Toshihide Hige, Allan Wong, Zhiyuan Lu, C Shan Xu, Patricia K Rivlin, Harald Hess, Ting Zhao, Toufiq Parag, et al. A connectome of a learning and memory center in the adult Drosophila brain. *Elife*, 6:e26975, 2017.

[57] Nobuaki K Tanaka, Hiromu Tanimoto, and KEI Ito. Neuronal assemblies of the drosophila mushroom body. *Journal of Comparative Neurology*, 508(5):711–755, 2008.

[58] Lin Tian, S Andrew Hires, Tianyi Mao, Daniel Huber, M Eugenia Chiappe, Sreekanth H Chalasani, Leopoldo Petreanu, Jasper Akerboom, Sean A McKinney, Eric R Schreiter, Cornelia I Bargmann, Vivek Jayaraman, Karel Svoboda, and Loren L Looger. Imaging neural activity in worms, flies and mice with improved GCaMP calcium indicators. *Nature Methods*, 6(12):875–881, November 2009.

[59] Tim Tully and William G. Quinn. Classical conditioning and retention in normal and mutant-Drosophila melanogaster. *Journal of Comparative Physiology A*, 157(2):263–277, March 1985.

[60] Glenn C. Turner, Maxim Bazhenov, and Gilles Laurent. Olfactory Representations by *Drosophila* Mushroom Body Neurons. *Journal of Neurophysiology*, 99(2):734–746, February 2008.

[61] Katrin Vogt, Christopher Schnaitmann, Kristina V Dylla, Stephan Knapek, Yoshinori Aso, Gerald M Rubin, and Hiromu Tanimoto. Shared mushroom body circuits underlie visual and olfactory memories in Drosophila. *eLife*, 3:e02395, August 2014.

[62] R. I. Wilson. Transformation of Olfactory Representations in the Drosophila Antennal Lobe. *Science*, 303(5656):366–370, January 2004.

[63] Zhihao Zheng, J Scott Lauritzen, Eric Perlman, Camenzind G Robinson, Matthew Nichols, Daniel Milkie, Omar Torrens, John Price, Corey B Fisher, Nadiya Sharifi, Steven A Calle-Schuler, Lucia Kmecova, Iqbal J Ali, Bill Karsh, Eric T Trautman, John A Bogovic, Philipp Hanslovsky, Gregory S X E Jefferis, Michael Kazhdan, Khaled Khairy, Stephan Saalfeld, Richard D Fetter, and Davi D Bock. A Complete Electron Microscopy Volume of the Brain of Adult Drosophila melanogaster. *Cell*, 174(3):730–743.e22, July 2018.

Supplementary Material

Details of Electrophysiology

Sample	$Vm[mV]$	$R_s[M\Omega]$	$R_{in}[M\Omega]$	$R_m[M\Omega]$	$R_{seal}[M\Omega]$	$\tau[ms]$	$C_m[pF]$	$C_{spec}[\mu F/cm^2]$	$C_{pass}[S/cm^2]$
Cell 1	-52.8	87.2	1066	979	NA	15.5	15.83	0.257	0.0000166
Cell 2	-63.1	74.5	998	924	NA	12.2	13.21	0.214	0.0000176
Cell 3	-52.3	36.4	801	765	1200	15.9	20.79	0.337	0.0000212
Cell 4	-59.2	75.2	942	866	1100	10.7	12.35	0.200	0.0000187
Cell 5	-56.2	45.4	1143	1097	1000	23.7	21.60	0.350	0.0000148
Mean	-56.7	63.7	990	926	1100	15.6	16.76	0.272	0.0000178
SD	4.5	21.7	130	124	100	5.0	4.26	0.069	0.0000024
SEM	2.0	9.7	58	55	45	2.3	1.90	0.031	0.0000011

Table S1: Passive membrane properties of MBON-α3 calculated from electrophysiological measurements.

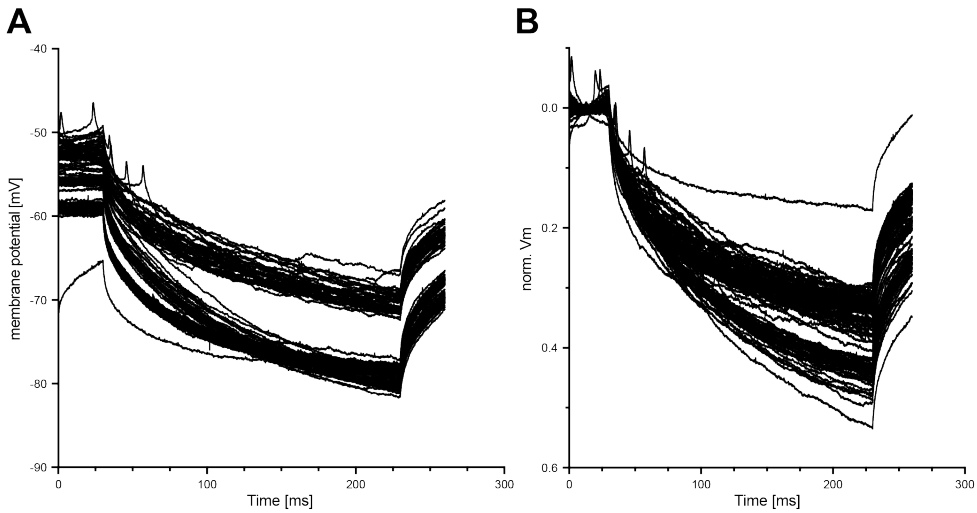

Figure S1: Raw traces from electrophysiological recordings of MBON-α3. (A) Raw traces of the induced membrane polarization through a $200ms$ long current injection of $-10pA$. We combined 35 trials of 3 different cells for the characterisation of the membrane time constant τ (B) Same, but normalised.

Details of Model Implementation

Morphological Parameters

Parameter	Value
number of sections	4342
average section length	$1.2384603363683644\mu m$
total length	$5377.394780511431\mu m$
average diameter	$0.2932798907665771\mu m$
average segment surface area	$1.2639994916933688\mu m^2$
total surface area	$6168.31751946371\mu m^2$
soma diameter	$6.45\mu m$

Table S2: Whole model morphological parameters

Physiological Parameters

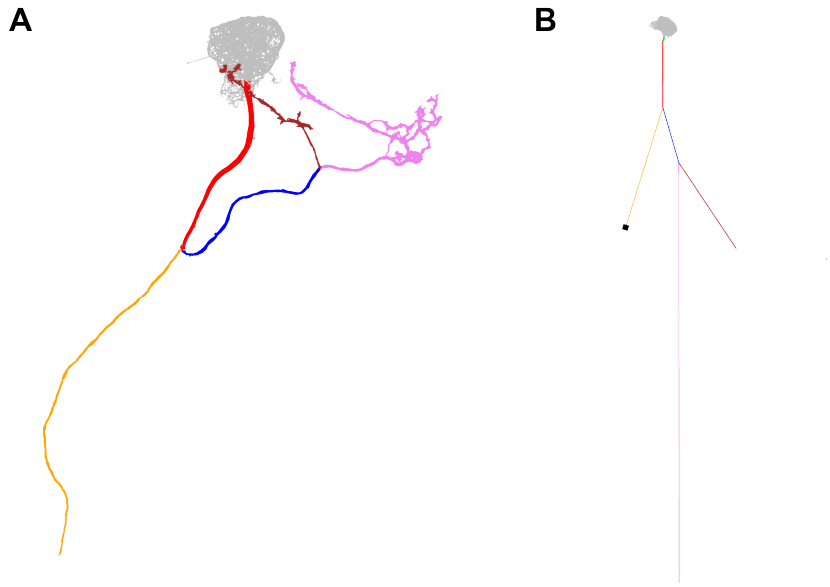

(a) Color coded electron microscopy based reconstruction (A) and *in silico* model (B) to illustrate the appended sections and the corresponding diameter and lengths.

Section	**Length**[μm]	**Diameter**[μm]	**Number of Segments**
Neurite 1 (red)	75.8877	1.1383	27
Neurite 2 (orange)	151.5752	0.6326	39
Branch 1 (blue)	65.9758	0.6860	17
Branch 2 (violet)	480.3213	0.8015	363
Branch 3 (brown)	129.0176	0.7913	97
Soma	6.4539	6.4539	1

Figure S2: Detailed overview of implemented segments from electron microscopy in the *in silico* model. Each section of the model is listed with the corresponding length, diameter and number of semgents, where the latter corresponds to NEURON's 'nseg' variable in constructing each section.

Electrophysiological Properties					
Variable	**Description**	**Fitted**	**Literature**	**Measured**	**Notes**
R_a (Ra)	Cytoplasm resistivity [Ω×cm]	85.41	30-400	926 ±55	ref. [7]
C_m (cm)	Specific membrane capacitance [μF/cm^2]	0.6961	0.6-2.6	0.27 ±0.03	ref. [7]
g_{pas} (pas.g)	Passive membrane conductance [S/cm^2]	$9.399 * 10^{-6}$	$3.8 * 10^{-5} - 1.2 * 10^{-4}$		
e_{pas} (pas.e)	Leak reversal potential [mV]	-55.64	-60	-56.7 ±2.0	ref. [5]
Synaptic Parameters					
τ (tau)	time to max. conductance [ms]	N.A.	0.44		ref. [52]
E	synaptic current reversal potential [mV]	N.A.	8.9		ref. [52]
$G_{max}(gmax)$	maximal conductance [μmho]	N.A.	$1.5627 * 10^{-5}$		Determined to achieve the target MBON depolarization from monosynaptic KC innervation ref. [24]

Table S3: Electrophysiological properties of the Drosophila MBON-α3-A *in silico* model. Parameter values are obtained either directly from the literature or, where necessary, calculated based on available data, as noted. The first column shows as parentheticals the parameter names used in the NEURON environment.